Article:

Shen, Lu, Zakharov, Yury orcid.org/0000-0002-2193-4334, Henson, Benjamin et al. (3 more authors) (2024) Target Detection Using Underwater Acoustic Communication Links. IEEE Journal of Oceanic Engineering. 10709868. ISSN 0364-9059

https://doi.org/10.1109/JOE.2024.3455414

Target detection using underwater acoustic communication links

Lu Shen*, Yuriy Zakharov*, Benjamin Henson*, Nils Morozs*,
Benoît Parrein†, Paul D. Mitchell*
*School of Physics, Engineering and Technology, University of York, U.K
†Nantes Université, Polytech Nantes, CNRS, LS2N, F-44000 Nantes, France

Abstract

Underwater monitoring and surveillance systems are essential for underwater target detection, localization and classification. The aim of this work is to investigate the possibility of target detection by using data transmission between communication nodes in an underwater acoustic (UWA) network, i.e, re-using acoustic communication signals for target detection. A new target detection method based on estimation of the time-varying channel impulse response between the communication transmitter(s) and receiver(s) is proposed and investigated. This is based on a lake experiment and numerical experiments using a simulator developed for modeling the time-varying UWA channel in the presence of a moving target. The proposed detection method provides a clear indication of a target crossing the communication link. A good similarity between results obtained in the numerical and lake experiments is observed.

Index Terms

distributed networks, lake experiment, target detection, underwater acoustics

I. INTRODUCTION

Underwater monitoring and surveillance systems are essential for underwater target detection, localization and classification. Dedicated passive and active sonar systems are commonly used for this purpose. The detection performance of passive systems is limited when the acoustic sound produced by the target is of a low intensity, in which case active sonars, monostatic or bistatic, are preferable. Monostatic sonars are based on backscattering of acoustic signals from the target. It is however known that the forward scattering from the target, exploited in bistatic sonars, may have a higher intensity [1].

Active multiple-input multiple-output (MIMO) sonar systems can significantly improve target detection performance [2], [3]. When the number of MIMO links is large, it is possible to detect the target with a single MIMO snapshot [2].

A number of lake experiments were conducted between 1997 and 1999 to investigate methods of detecting forward scattering from a moving target [4], [5]. In these experiments, tone signals are simultaneously transmitted at a set of carrier frequencies within the frequency range 1–3 kHz. A signal source fixed at the lake bottom or a vertical antenna array is used for transmission. Both vertical and horizontal receiving arrays are deployed at a distance of about 400 m. Targets of several meters in length and up to 1 m height are towed underwater across the area between the transmitter and receiving arrays. The aim is to detect the diffracted signals against the fluctuating direct signal. In [4], fluctuations of the direct signal are removed by a high-pass filter, the cut-off frequency of which is computed based on *a priori* information, including the size and velocity of target. The signal then goes through a filter matched to a theoretical model of the diffracted signal, it is accumulated over the array elements and averaged over frequency. The target detection is performed based on the variation of the output signal. The performance is evaluated by the output signal-to-noise ratio ($\mathrm{SNR}_{\mathrm{out}}$) which is defined as the ratio between an increment in the output signal and the standard deviation of the output signal without a target. It is found in [5] that $\mathrm{SNR}_{\mathrm{out}}$ can be improved by jointly processing the output signals of two vertical arrays. Another finding is that it is possible to indicate the direction of the target movement based on the shape of the peaks in the processed signal. A comparative analysis of detection methods is conducted in [6] using the experimental data described in [4], [5]. It is found that the use of a vertical array shows more robust target detection performance compared to a horizontal array. Further analysis is conducted in [7] to investigate the detection performance with coherent, partially coherent and incoherent spatial processing. It is indicated that the choice of spatial processing method depends on the vertical distribution of the acoustic field. Sea trials are conducted to investigate the performance of underwater acoustic barriers based on forward scattering in [8]. The configuration of the experiment includes an array of acoustic projectors and a hydrophone array. During the experiment, pulses of a 15 kHz sine wave are transmitted. Moving objects are towed between the source and hydrophone arrays. Target detection and localization are performed based on the shadowing of acoustic field caused by the moving object. Aforementioned works focus on investigating matched filtering/time reversal based methods for detecting the forward scattering from a target using transmit and/or receive antenna array and low-frequency pulse transmission.

In [9], an adaptive cancellation algorithm is applied to the received signals to enhance the detection of forward scattering from the strong direct path in a lake experiment. The source is located at 4 m depth. A vertical array with 10 hydrophones is deployed at a distance of 900 m. The dimension of the target is 6 m×1 m. Successive pulses at a 10 kHz carrier frequency are transmitted. An adaptive filter is used for signal processing. The input of the adaptive filter is a segment of a signal received when the target is absent. Other segments of the received signal are used as the desired signal, with which the filter output is compared to produce the adaptive filter error. As the forward scattered signal is weakly correlated with the direct signal, it is assumed that the algorithm will only cancel the direct signal, and the adaptive filter error will be higher when the target is present. This method also requires a vertical antenna array.

In this work, we consider scenarios with a distributed network of multiple unsynchronized acoustic sensor nodes capable of communicating with each other, instead of using source/receiver arrays. Such a network provides flexibility in the deployment of the acoustic sensor nodes based on the environment. Wideband acoustic signals at a relatively high frequency (32 kHz carrier frequency in our experiments) are used for data transmission. The aim of this work is to investigate the possibility of re-using the communication signals in the network for target detection. The target detection is performed based on the measurement of the time-varying channel impulse responses (CIRs) between communication nodes in the network. Note that the channel estimation, i.e. CIR measurement, is one of the main steps of signal processing in the receiver, hence a CIR estimate is normally available at the receiver. The idea is to detect changes in the CIR caused by the target movement. The use of wideband signal provides high resolution CIRs, which increases the chance of target detection. In this paper, we focus on the target detection performed for each individual network link. Designs of multiple access control and network layer protocols for such a target detection network are presented in [10], [11].

Fig. 1 illustrates a scene of a distributed network with six Tx/Rx nodes and a target. We consider the scenario when there is a 'silent' target moving underwater. When the target is absent, the acoustic multipath propagation from node A to node B only includes the node-to-node link. When there is a target, apart from the link between two nodes, scattering from the target will also be present. The acoustic propagation between two nodes in the presence of the target will correspond to a different CIR compared to the 'no target' case. Therefore, it is possible to perform target detection based on changes in the CIR in time. A challenge is to distinguish

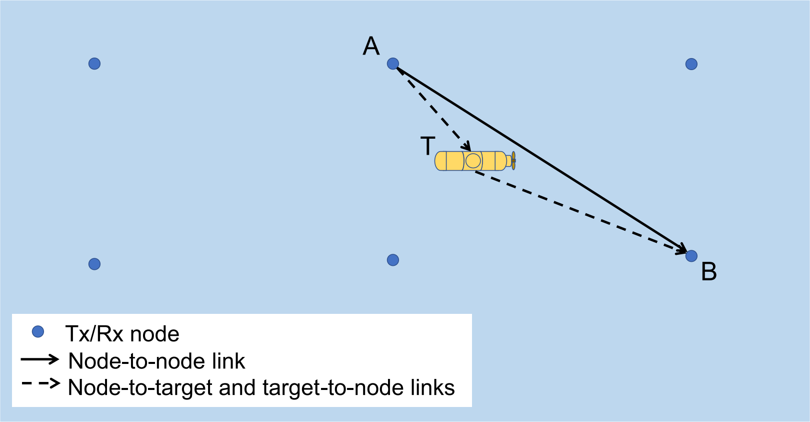

Fig. 1: Acoustic propagation between two nodes (A and B) with presence of a target (T) in a distributed network (Top view).

between changes in the CIR due to environmental factors, such as node drift or surface waves, and change caused by a moving target. To this end, a detection algorithm is proposed in this paper which reduces the impact of environmental variations on the CIR and subsequent detection performance.

For performance evaluation of the target detection scheme, an acoustic simulator for conducting virtual signal transmission experiments is developed; it is capable of modelling the multipath propagation and Doppler effects for different UWA environments taking into account the motion of the transmitter/receiver/target. One of the key requirements of the simulator is to generate highly accurate acoustic field information for the communication links based on the trajectories of the nodes and the target. Unlike the typical static/slowly moving transmitter and receiver nodes, the target might be moving at a high speed. To track the fast variation of the acoustic channel, a high CIR sampling rate is required. Therefore, the simulator computes the acoustic field at the baseband sampling interval of the communication signals. To reduce the computational time, the simulator exploits the principles of the Waymark and VirTEX simulators [12], [13], where the acoustic field is pre-computed within an area of interest on a grid of space points and then interpolated based on the pre-computed information.

The field interpolation method proposed in [13] assumes that the receiver is in the far field with respect to the signal source. However, the target can reflect/re-radiate a transmission and could be positioned closely to the communication nodes, thus the interpolation method used in [12], [13] might not be accurate enough. To improve the field interpolation in the near field, an improved interpolation approach is proposed. The proposed simulator is used to generate the time-varying CIR and the signal at the receiver. The simulator is used for evaluating the detector performance.

To verify the target detection performance and validate the simulator, a lake experiment is conducted with several nodes and a target whose trajectory is accurately estimated using acoustic navigation. In the lake experiments, the CIR estimates are obtained from the channel estimator in the receiver and then used for the target detection. After the lake experiment, we run the simulator with the same node configuration, and use the target trajectory estimate as input to generate the CIRs and received signals. A good match between the experimental and simulation results is observed.

The contributions of this paper are as follows.

- A target detection algorithm is proposed based on measuring changes in the time-varying CIRs between communication nodes, which are estimated using the existing communication signals in the network.
- An acoustic simulator is developed, which takes into account the motion of the target and the communication nodes. The output of the simulator includes the signals received at nodes and time-varying CIRs between each transmitter-receiver pair. An approach is proposed and implemented to improve the acoustic field interpolation in the near field. The simulator is validated using the lake experiment.
- With the help of the simulator, the performance of the proposed algorithm is evaluated in the form of ROC (receiver operating characteristic) curves. The CIR sampling (packet transmission) rate is also analyzed.
- The performance of the proposed detection method is investigated in lake experiments.

The structure of the paper is as follows. Section II describes the target detection algorithm. Section III introduces the acoustic simulator. Section IV describes the acoustic field interpolation approaches. Numerical simulation and lake experiments are presented in Section V and VI, respectively. The conclusions and discussion are given in Section VII.

II. TARGET DETECTION BASED ON CIR VARIATION

The key idea of target detection is to identify changes in the CIR caused by a moving target. The changes in the CIR can be measured by the mean squared deviation (MSD) [14]:

$$\text{MSD} = \sum_{n=0}^{L-1} |h_0(n) - h(n)|^2, \tag{1}$$

where L is the length of the CIR, n is the index of the channel delay tap, h_0 is a reference CIR when the target is absent, and h is the CIR obtained at a time interval where a target might be present. The MSD in (1) can be computed using the frequency-domain representation of the channel:

$$\text{MSD} = \sum_{k=0}^{K-1} |H_0(k) - H(k)|^2, \tag{2}$$

where H_0, H are the frequency responses of filters h_0 and h, respectively, and they are computed using the fast Fourier Transform (FFT) of a size K. When the MSD is lower than a detection threshold, we can assume that the target is absent. For MSD values higher than the threshold, we can assume that the target is present.

However, even when the target is absent, the CIR will be time-varying due to the time-varying nature of the UWA channel, thus resulting in a high MSD (false alarm). Therefore, we need to distinguish between the change of the impulse response due to the time-varying environment and the change caused by a moving target. Instead of using h_0 in (1), we can use $h_0 * g$, where $*$ denotes the convolution operation and g is an impulse response representing a filter with a small delay spread. In such a case, the change in delay and amplitude caused by the slow motion of the source and the receiver, the variations of the environment and the clock mismatch between the transmitter and the receiver can be eliminated from influencing the MSD. When a target is crossing the communication link, the multipath structure of the propagation channel will change significantly, and these changes cannot be compensated by the filter g.

Small delays introduced by the filter g in the time domain correspond to complex exponentials of long periods in the frequency domain. Therefore, the frequency response of g can be expressed as a combination of complex exponentials with expansion coefficients $c(p)$ [15]:

$$G(k) = \sum_{p=0}^{2P} c(p) e^{j2\pi(-P+p)k/K}, \; k = 0, \ldots, K-1, \tag{3}$$

where the number of complex exponentials $2P+1$ corresponds to the delay spread of the filter g.

Therefore, to find the filter g, we solve the following optimization problem:

$$\hat{G} = \underset{G}{\operatorname{argmin}} \sum_{k=0}^{K-1} |H_0(k)G(k) - H(k)|^2. \tag{4}$$

We denote the combined frequency response as:

$$\begin{aligned} \tilde{H}(k) &= H_0(k)G(k) \\ &= \sum_{p=0}^{2P} c(p)\tilde{G}(k,p), \end{aligned} \tag{5}$$

where $\tilde{G}(k,p) = H_0(k)e^{j2\pi(-P+p)k/K}$, and find the expansion coefficients $\mathbf{c} = [c(0),\ldots,c(2P)]^T$ by minimizing the cost function:

$$J(\mathbf{c}) = \sum_{k=0}^{K-1} |\tilde{H}(k) - H(k)|^2. \tag{6}$$

The classical least squares solution can be found by the normal equation [16]:

$$(\mathbf{R} + \epsilon\mathbf{I})\mathbf{c} = \mathbf{b}, \tag{7}$$

where $\mathbf{I}$ is an identity matrix, $\mathbf{R} = \tilde{\mathbf{G}}^H\tilde{\mathbf{G}}$, $\mathbf{b} = \tilde{\mathbf{G}}^H\mathbf{H}$, $\tilde{\mathbf{G}}$ is a $K \times (2P+1)$ matrix with elements $\tilde{G}(k,p)$, $\mathbf{H} = [H(0),\ldots,H(K-1)]^T$ and $\epsilon > 0$ is a regularization parameter. The regularization parameter ϵ is introduced to avoid the numerical instablity due to the matrix inversion. In this paper, ϵ is set as $10^{-3} \times \max\{\text{diag}[\mathbf{R}]\}$, where $\max\{\text{diag}[\mathbf{R}]\}$ is the maximum diagnal element of $\mathbf{R}$. The solution of (7) is given by:

$$\hat{\mathbf{c}} = (\mathbf{R} + \epsilon\mathbf{I})^{-1}\mathbf{b}. \tag{8}$$

After obtaining $\hat{\mathbf{c}}$, we have $\tilde{H}(k) = \sum_{p=0}^{2P} \hat{c}(p)\tilde{G}(k,p)$. The deviation in the frequency response is computed as: $\Delta H(k) = \tilde{H}(k) - H(k)$. Finally, the normalized MSD is computed by:

$$\text{MSD}_{\text{norm}} = \frac{\|\Delta H(k)\|_2^2}{\|H_0(k)\|_2 \|H(k)\|_2}, \tag{9}$$

where $\|\cdot\|_2$ denotes the Euclidean norm.

The normalized MSD is used as the statistic for the target detection. The decision is made based on a detection threshold Γ. When the normalized MSD is lower than Γ, it means that the communication link is not distorted, i.e, the target is absent. When it is higher than Γ, it can be inferred that the link distortion is caused by a target. With a dataset of CIRs obtained without a target, the probablity of false alarm can be computed for a set of threshold values. The detection threshold can then be chosen based on an acceptable false alarm probability.

In practice, using one CIR as the reference might not be sufficient for target detection in fast time-varying channels. To reduce the impact of the channel variation on the detection performance, the normalized MSD is computed Q times with different reference CIRs. These reference CIRs should cover the uncertainty area caused by the channel variation due to the changing environment. The minimum normalized MSD among Q measurements is kept as the final normalized MSD. The higher the channel uncertainty, the higher Q should be used. The detection algorithm can be summarized as:

$$\xi = \min_{q\in[1,Q]} \{\min_{\mathbf{c}} J(\mathbf{c})\} \underset{\text{No target}}{\overset{\text{Target detected}}{\gtrless}} \Gamma. \tag{10}$$

III. SIMULATOR FOR ACOUSTIC LINKS

Underwater acoustic channel simulators, such as Waymark [12], [17], [18], can model the signal transmission with a moving transmitter and receiver. To reduce the computational complexity, the acoustic field is sampled at an interval, which is typically significantly longer than the baseband sampling interval [12], [18]. In this work, we introduce a moving target crossing the communication links, and to guarantee accurate modelling of the signal transmission in the presence of a fast-moving target, the acoustic field is computed at the baseband sampling rate. Even at baseband frequencies, generating the acoustic field for prolonged scenarios can be impractical for meaningful numerical experiments. Therefore, the simulator exploits the principles used in [12], [13] and performs the task in two stages: pre-processing and received signal computation.

A. *Pre-processing*

The acoustic field between a pre-defined source position and possible receiver positions within an area of interest on a predefined set of grid points is pre-computed. The BELLHOP3D ray-tracing program [19] is used to generate the acoustic field information, including the delay τ, amplitude A, departure angle θ_d and incident angle θ_i of each arrival for each grid point. We consider a simplified environment with a flat surface, flat bottom and range-invariant sound speed profile. The pre-computation is performed for a set of source depths required to cover the range of possible source depths. For each source depth, acoustic field computation is performed on a two-dimentional (depth, range) grid map of receiver positions. For the source parameters, the anticipated source positions and target trajectories define the minimum depth, the maximum

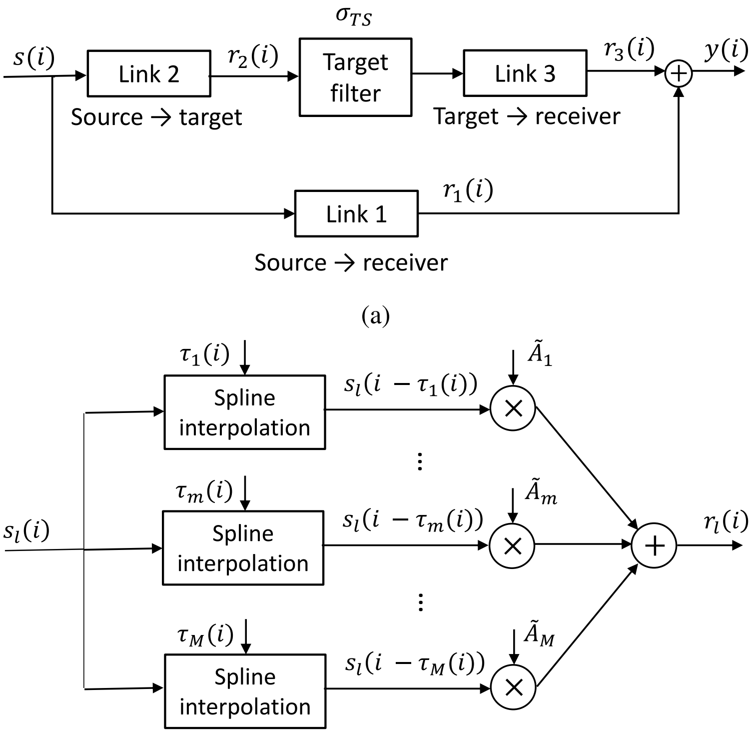

(a)

(b)

Fig. 2: General structure of the simulator: (a) Received signal computation; (b) Filtering for the lth link, $l = 1, 2, 3$, i is the index of the baseband sample, where s_l is the baseband input signal and r_l is the baseband output.

depth and the resolution (step size) in depth ΔD_s. The parameters of the grid map include the minimum and maximum range, the minimum and maximum depth, and the resolution of the grid map in range and in depth.

B. Received signal computation

To obtain the received signal, the acoustic propagation of three links need to be considered as illustrated in Fig. 2a. Link 1 is the direct link between the source and the receiver when the target is absent; Link 2 is the link between the source and target; and Link 3 is the link between the target and receiver. The target plays the role of a receiver when modelling link 2, and it acts as a source when modelling link 3. A target filter is used to incorporate a target strength model [20].

The acoustic fields of all three links are computed by acoustic field interpolation. The trajectories of the source, receiver and target are interpolated to the baseband sampling rate. The field interpolation is performed according to the source, target and receiver positions with respect to the closest grid points within the grid maps using the field information at these grid points. More details on the acoustic field interpolation are given in Section IV.

As shown in Fig. 2b, the output of the lth link is the signal:

$$r_l(i) = \sum_{m=1}^{M} \tilde{A}_m(i) s_l(i - \tau_m(i)), \tag{11}$$

where i is the index of a baseband sample, $s_l(i)$ is the baseband input of the lth link, M is the number of arrivals, $\tau_m(i)$ is the delay of the mth arrival obtained from the field interpolation, and $\tilde{A}_m(i)$ is the baseband equivalent amplitude of the mth arrival computed according to beampatterns of the source and receiver:

$$\tilde{A}_m(i) = G_s(\theta_d^m) G_r(\theta_i^m) A_m(i) e^{-j\omega_c \tau_m(i)}, \tag{12}$$

where $\omega_c = 2\pi f_c$, f_c is the carrier frequency of the transmitted signal, $A_m(i)$ is the amplitude of the mth arrival obtained from the field interpolation, G_s and G_r are the source and receiver beampatterns, θ_d^m is the departure angle of the mth arrival, θ_i^m is the incident angle of the mth arrival, obtained from the field interpolation. The baseband input sample $s_l(i-\tau_m(i))$ is obtained using the local spline interpolation as described in [17]. The signal at the receiver is then given by:

$$y(i) = r_1(i) + r_3(i). \tag{13}$$

In this paper, the target is modelled as a rigid sphere of radius a. The bistatic target strength can be written as a function of the angle $\alpha(i)$ between the incident and scattered rays. Here we compute $\alpha(i)$ as:

$$\alpha(i) = |\alpha_{\mathrm{ST}}(i) - \alpha_{\mathrm{TR}}(i)|, \tag{14}$$

where $\alpha_{\mathrm{ST}}(i)$ is the azimuth angle between the source and the target and $\alpha_{\mathrm{TR}}(i)$ is the azimuth angle between the target and receiver and $\alpha_{\mathrm{TR}}(i) \in (-\pi, \pi]$. Therefore, the target filter is modelled as a single-tap filter with a target strength coefficient [21]:

$$\sigma_{TS}(i) = \begin{cases} \dfrac{a^2}{4}\left[1 + \tan^2\left(\dfrac{\alpha(i)}{2}\right) J_1^2\left(wa\sin\alpha(i)\right)\right] & \alpha(i) \neq \pi \\ \dfrac{a^2}{4}(1 + w^2 a^2) & \alpha(i) = \pi \end{cases} \tag{15}$$

where $w = 2\pi/\lambda$ is the wavenumber, λ is the acoustic wavelength, $J_1(\cdot)$ is the Bessel function of the first order.

C. Channel impulse response computation

Apart from the signal at the receiver, the simulator also provides the time-varying CIR between the source and receiver. For every position of the signal source, receiver and target, the channel frequency response is computed as:

$$H(i,k) = H_1(i,k) + \sigma_{TS}(i) H_2(i,k) H_3(i,k), \tag{16}$$

where H_1, H_2, H_3 represent the baseband frequency responses of the three links in Fig. 2a. For instance, the frequency response $H_1(i,k)$ is computed as:

$$H_1(i,k) = \sum_{m=1}^{M} \tilde{A}_m(i) e^{-j2\pi k \Delta f \tau_m(i)}, \ \ k \in [-B/2, B/2], \tag{17}$$

where $B\Delta f$ is the frequency bandwidth, Δf is the frequency resolution. The channel impulse response $\mathbf{h}(i)$ is then computed using the inverse FFT of H.

IV. ACOUSTIC FIELD INTERPOLATION

For pre-computation, a set of grid maps are generated, each corresponding to a particular source depth. When the source/receiver is not on a grid point, acoustic field interpolation is performed. Plane wave acoustic field approximation works well when the receiver is in the far field of the signal source. In simulation scenarios, the target (as a receiver and signal source) can be arbitrarliy close to a node; in such cases, the spherical wave approximation improves the interpolation [22]. In this section, we present acoustic field interpolation based on plane wave and spherical wave approximations.

A. Source at a depth with precomputed grid map and receiver between grid points

We first consider a scenario when the source is at a depth for which a grid map has been precomputed and the receiver is located at a point (x, y) between grid points on the map.

1) Plane wave interpolation: In [13], a plane wave assumption is used for acoustic field interpolation as shown in Fig. 3. The arrivals at the receiver position (x, y) is the combination of the arrivals at the four neighbouring grid points $(x_a, y_b), a, b \in [1, 2]$, with weighted amplitudes and delay adjustments. The delays are adjusted by the difference in the wave travel time between the neighbouring points and the position of the receiver. Assuming that a ray is arriving at a grid point (x_a, y_b) with an incident angle θ_i, the difference in the travel time is given by [13]:

$$\Delta\tau = \Delta d / c = (\Delta x \cos(\theta_i) + \Delta y \sin(\theta_i))/c, \tag{18}$$

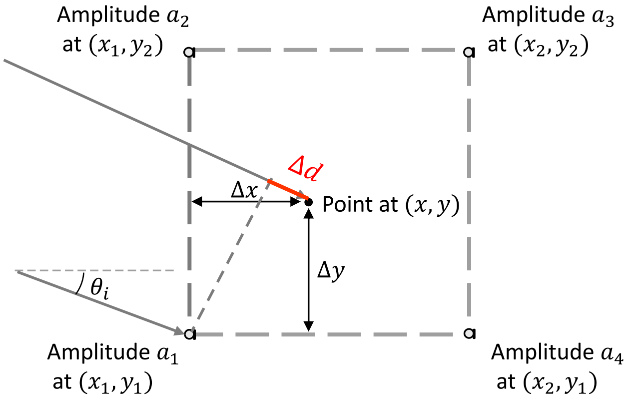

Fig. 3: An illustration of plane wave interpolation for a receiver position (x, y) based on the ray information at the grid point (x_1, y_1), where θ_i is the incident angle of a ray arriving at (x_1, y_1).

where c is the speed of sound, $\Delta x = x - x_a$ and $\Delta y = y - y_b$. Note that $\Delta\tau$ can be positive or negative. For a ray arriving with an incident angle of θ_i in Fig. 3, $\Delta\tau$ at (x, y) is positive when adjusting the delay of the ray (of the same incident angle) arriving at (x_1, y_1), while $\Delta\tau$ at (x, y) is negative when adjusting the delay of the ray arriving at (x_2, y_2). The delay of arrival for the mth ray from (x_a, y_b) is updated as: $\tau_m^{'} = \tau_m + \Delta\tau$.

The amplitude of the arrivals for the four neighbouring grid points are weighted by:

$$\begin{aligned} a_1 &: (1 - w_1)(1 - w_2), \\ a_2 &: (1 - w_1)w_2, \\ a_3 &: w_1 w_2, \\ a_4 &: w_1(1 - w_2), \end{aligned} \tag{19}$$

where a_1, a_2, a_3, a_4 represent amplitudes of the arrivals at the four grid points. The weights are computed based on the position of the receiver (x, y) with respect to the grid points:

$$\begin{aligned} w_1 &= (x - x_a)/(x_2 - x_1), \\ w_2 &= (y - y_b)/(y_2 - y_1). \end{aligned} \tag{20}$$

The main steps of the plain wave interpolation can be summarized as:

(i) Adjust the delay of the arrivals at four grid points based on (18).

(ii) Apply weighting to the amplitudes of the arrivals at four grid points according to (19) and (20).

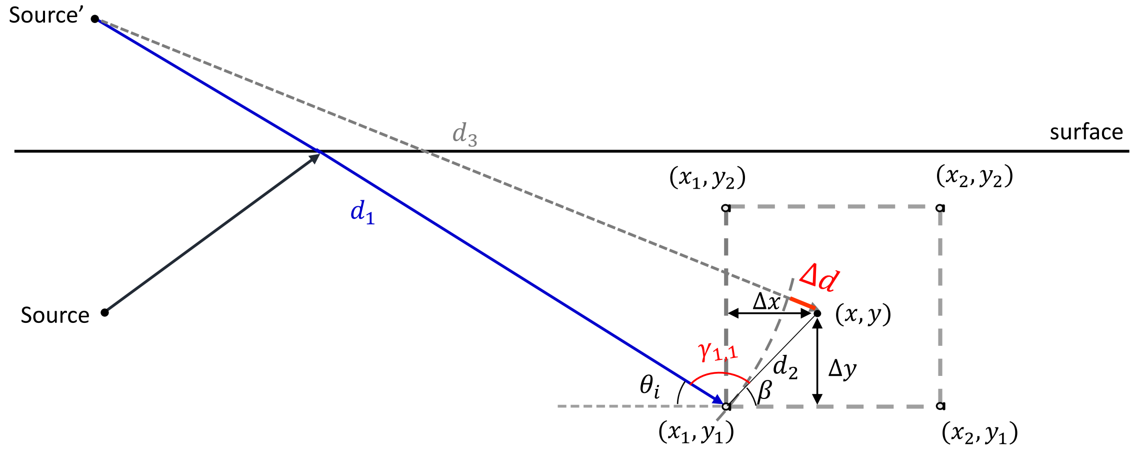

Fig. 4: An illustration of spherical wave interpolation for a receiver position (x, y) based on the ray information at the grid point (x_1, y_1), where Δd is the difference between d_3 and d_1, θ_i is the incident angle of a ray arriving at (x_1, y_1), $\gamma_{1,1}$ is the angle between d_1 and d_2, and β is the angle bewteen d_2 and x positive axis.

2) Spherical wave interpolation: An illustration of delay adjustment when using spherical wave approximation is shown in Fig. 4. As the delay adjustment for a direct path is straightforward, we use a surface reflection as an example. The same procedure applies for the bottom reflections.

We first find the image source position $(\text{Source}^{'})$ using the image source method (ISM) [23]. As shown in Fig. 4, d_1 is the distance a ray travels to arrive at (x_1, y_1) and d_3 is the distance it needs to travel to arrive at (x, y). The delay adjustment is made based on the difference between d_1 and d_3.

For the mth arrival at a grid point (x_a, y_b), the distance between the image source position and the grid point can be computed as: $d_1 = c\tau_m$, where τ_m is the delay of the mth arrival. The distance between the receiver position (x, y) and (x_a, y_b) can be found as: $d_2 = \sqrt{(\Delta x)^2 + (\Delta y)^2}$. By denoting the angle between d_1 and d_2 as $\gamma_{a,b}$, and assuming the angle to be known, distance d_3 can be computed based on the cosine rule as:

$$d_3 = \sqrt{d_1^2 + d_2^2 - 2d_1 d_2 \cos\left(\gamma_{a,b}\right)}. \tag{21}$$

Thus, we can obtain the change in the delay τ_m as:

$$\Delta\tau = \Delta d/c = (d_3 - d_1)/c, \tag{22}$$

and the delay of the mth arrival at (x, y) can be updated as: $\tau_m^{'} = \tau_m + \Delta\tau$.

The angle $\gamma_{a,b}$ can be computed using the incident angle of the arrival θ_i and the angle between d_2 and x positive axis (denoted as β). Note that the incident angle θ_i is within $[-\pi/2, \pi/2]$. For a grid point (x_a, y_b):

$$\beta = \arctan\left(\frac{|y - y_b|}{|x - x_a|}\right). \tag{23}$$

For the four grid points, we have:

$$\begin{aligned}
\gamma_{1,1} &= \begin{cases} \pi - \text{sign}(\theta_i + \beta)(\theta_i + \beta) & \theta_i < 0 \\ \pi - (\theta_i + \beta) & \theta_i \geq 0 \end{cases} \\
\gamma_{1,2} &= \begin{cases} \pi - \text{sign}(\theta_i - \beta)(\theta_i - \beta) & \theta_i > 0 \\ \pi + \theta_i - \beta & \theta_i \leq 0 \end{cases} \\
\gamma_{2,1} &= \begin{cases} \text{sign}(\theta_i - \beta)(\theta_i - \beta) & \theta_i > 0 \\ \theta_i - \beta & \theta_i \leq 0 \end{cases} \\
\gamma_{2,2} &= \begin{cases} \text{sign}(\theta_i + \beta)(\theta_i + \beta) & \theta_i < 0 \\ \theta_i + \beta & \theta_i \geq 0 \end{cases}
\end{aligned} \tag{24}$$

The amplitudes of the arrivals are weighted according to (19) and (20).

B. Source at a depth without precomputed grid map and receiver at a grid point

Now we consider the scenario when a source depth deviates from the source depth, for which a grid map exists, and the receiver position is on a grid point of the map. The idea is to adjust the delay of each arrival based on the deviation of the source depth from the nearest source depth with a precomputed grid map.

1) Plane wave interpolation: As illustrated in Fig. 5a, the difference in the travel time can be computed as:

$$\Delta\tau = -\Delta D \sin(\theta_d)/c, \tag{25}$$

where $\Delta D = D_{\text{off}} - D_{\text{on}}$, D_{off} is a source depth not with a pre-computed grid map and D_{on} is the nearest source depth with a grid map.

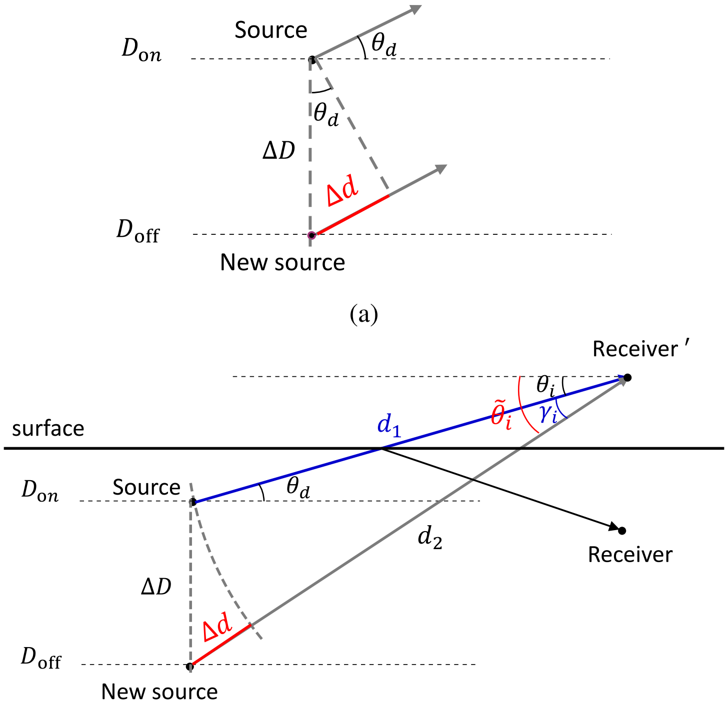

(a)

(b)

Fig. 5: Illustrations of interpolation schemes for new source depth based on the ray information at the known source depth; (a) plane wave interpolation, θ_d is the departure angle of a ray travelling from the original source; (b) spherical wave interpolation, Δd is the difference between d_2 and d_1, and $\tilde{\theta}_i$ is an incident angle due to the change in source depth.

2) Spherical wave interpolation: We first find the image receiver position based on ISM as shown in Fig. 5b. Assuming that there is a ray from the depth D_{on} with a departure angle of θ_d arriving at the receiver with a delay τ_m, the distance d_1 between the source and the image receiver can be computed as: $d_1 = \tau_m c$. Based on the cosine rule, we have:

$$d_2 = \begin{cases} \sqrt{d_1^2 + (\Delta D)^2 - 2d_1|\Delta D|\cos(\pi/2 - \theta_i)} & \theta_d > 0, \\ \sqrt{d_1^2 + (\Delta D)^2 - 2d_1|\Delta D|\cos(\pi/2 + \theta_i)} & \theta_d \leq 0. \end{cases} \tag{26}$$

The delay can be computed as:

$$\tau_m^{'} = \tau_m + \Delta\tau = \tau_m + (d_2 - d_1)/c. \tag{27}$$

For the plane wave approximation, the incident angle remains the same when there is a deviation in source position. However, for spherical wave approximation, there will be a change in the incident angle as illustrated in Fig. 5b. The new incident angle $\tilde{\theta}_i$ is computed based on the angle γ_i between d_1 and d_2. The angle γ_i is given by:

$$\gamma_i = \arccos\left(\frac{d_1^2 + d_2^2 - |\Delta D|^2}{2d_1 d_2}\right). \tag{28}$$

Finally, $\tilde{\theta}_i$ is computed as:

$$\tilde{\theta}_i = \theta_i + \text{sign}(\theta_i)\text{sign}(\Delta\tau)\gamma_i. \tag{29}$$

C. Arbitrary position of source and receiver

Now we consider the general scenario when both the source and the receiver positions deviate from a known depth/grid point.

The main steps of interpolation are:

1) Adjust delays of the arrivals at the four grid points based on the deviation of the source depth. For spherical interpolation, use (26) and (27). For plane wave interpolation, $\Delta\tau$ is computed using (25).
2) For the spherical interpolation only, adjust the incident angles of the arrivals at four grid points based on the deviation of source depth using (28) and (29).
3) Adjust delays of the arrivals based on the receiver position between grid points. For spherical interpolation, use (21) - (24). For plane wave interpolation, use (18).

In subsection IV-A and IV-B, we consider specific circumstances when the source/receiver is at a known depth/grid point to breakdown the description of the calculations for arbitary source/receiver positions. In practice, for any source and receiver positions, we follow the interpolation steps summarized in this subsection.

V. NUMERICAL SIMULATION

In this section, we investigate the performance of the acoustic field interpolation and show an example of the time-varying CIR when a target crosses a link between a signal source and receiver. The performance of the proposed detector is evaluated using ROC curves. The CIR sampling (packet transmission) rate is also analyzed.

A. Acoustic field interpolation

In this subsection, the performance of the plane wave and spherical wave acoustic field interpolation methods are compared.

We consider an environment with a flat surface and a flat bottom. The sea depth is 200 m, and the sound speed profile is the same as in the SWellEx-96 experiment [24]. Six grid maps are pre-computed for source depths from 15 m to 20 m with a depth step size of $\Delta D_s = 1$ m. The signal source depth in the simulation trials is random and independently uniformly distributed within $[15, 20]$ m. Each grid map covers the receiver range from 1 m to 50 m and receiver depths from 5 m to 40 m. The resolution of the grid maps in both range and depth is 0.5 m. In every simulation trial, the receiver range and depth are independent and uniformly distributed within $[15, 20]$ m and $[5, 40]$ m, respectively.

The interpolation accuracy is evaluated by computing the mean squared deviation:

$$\mathrm{MSD}_{\text{interp}} = \frac{||\mathbf{h} - \hat{\mathbf{h}}||_2^2}{||\mathbf{h}||_2^2},$$

where $\hat{\mathbf{h}} = [\hat{h}(0), \ldots, \hat{h}(K-1)]^T$ is a CIR estimate and $\mathbf{h} = [h(0), \ldots, h(K-1)]^T$ is the true CIR.

The CIR estimate and the true CIR are computed as the inverse FFT of the channel frequency response with the interpolated and true field information, respectively. The interpolated channel frequency response is computed using (16) and (17). For computation of the true CIR, the amplitude and delay of arrivals are generated at the precise positions of the source and receiver by running the BELLHOP3D program. For the CIR estimates, the acoustic field is computed using the plane or spherical wave interpolation as described in Section IV. In the simulations, the carrier frequency is $f_c = 32$ kHz and the frequency bandwidth is $F_d = 6$ kHz. In total, 10000 simulation trials are run.

Fig. 6a shows the cumulative distribution function (CDF) of the $\mathrm{MSD}_{\text{interp}}$ when using the plane wave and spherical wave interpolation. It can be seen that the performance of the spherical wave interpolation is significantly better than that of the plane wave interpolation. An $\mathrm{MSD}_{\text{interp}}$ better than -15 dB is achieved in 99% of the simulation trials for the spherical interpolation, while only in 86% of the simulation trials for the plane wave interpolation.

In Fig. 6a, the spherical interpolation shows a significantly better performance than the plane wave interpolation when the receiver is close to the signal source (range smaller than 50 m). To investigate the performance at a longer distance, we generate a single grid map at 20 m source depth for a longer range scenario. The signal source depth is randomly chosen within $[19.5, 20.5]$ m. The range of the receiver varies from 1000 m to 1030 m, and its depth varies from 15 m to 25 m. The resolution of the grid map in range and depth are both 1 m. Again, the

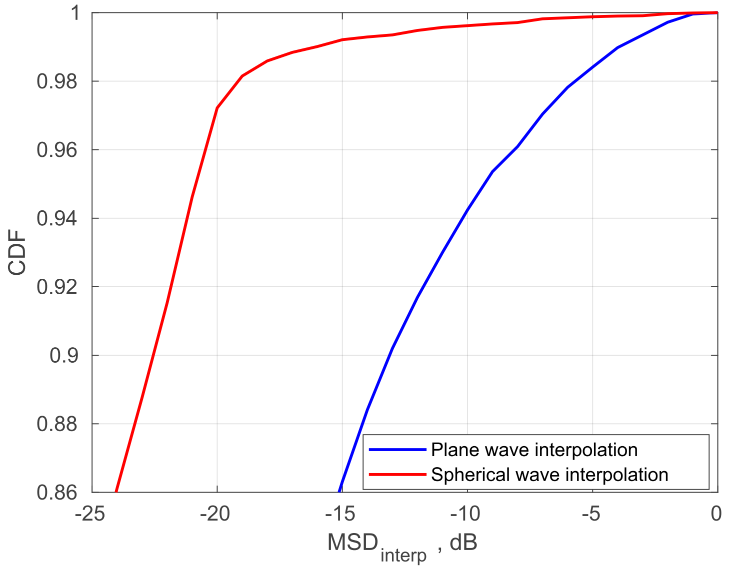

(a)

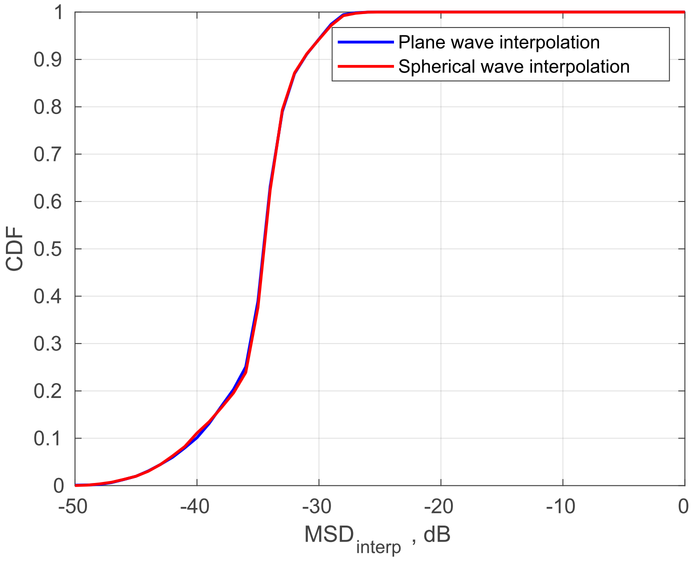

(b)

Fig. 6: CDF of $\mathrm{MSD}_{\text{interp}}$ for plane wave and spherical wave interpolation: (a) the receiver is at a short range (within 50 m from the signal source); (b) the receiver is at a long range (further than 1000 m away from the signal source).

receiver position is randomly chosen to be within the grid map. In total, 5000 simulation trials are run. As expected and demonstrated in Fig. 6b, almost the same performance is achieved by both plane wave and spherical wave interpolation.

To conclude, the spherical interpolation is accurate regardless of the range between the source and receiver, which is not the case for the plane wave interpolation. As the trajectory of the target can be close to the source or receiver, the spherical interpolation is a better candidate for the acoustic field interpolation.

B. Time-varying channel impulse response

In this subsection, we show an example of the time-varying CIR generated by the simulator using the spherical wave interpolation when the target is moving between the signal source and receiver.

This simulation scenario is set up based on one of the communication links in a lake experiment described in Section VI. For the simulation, we use the first 355 s of the estimated target trajectory in the lake experiment (see Fig. 17 in Section VI). The target is moving at a speed of 1 m/s at 1.5 m depth. The distance between two nodes is 14.2 m. The depth of the lake is set as 7 m. The transmitter is at 4.6 m depth and the receiver is at 4.4 m depth. In this simulaton, two grid maps are generated for a source depth of 1.5 m and 4.6 m depth. For each grid map, the range of the receiver varies from 0 to 35 m, and its depth varies from 0 to 7 m. The resolution of the grid map in range and depth is 1 m and 0.5 m, respectively. As described in Section III-C, the CIR is computed as the inverse FFT of the channel frequency response, given by (16). The CIR variation is due to the second term in (16), where both the links, link 2 and link 3, have time-varying channels. The magnitude of the CIR variation depends on the target strength σ_{TS}, which is computed using (15). For the purpose of observing the additional reflections introduced by the moving target, we set $\sigma_{\mathrm{TS}}(i) = 1$, i.e., at a high value, to highlight these reflections in the CIR. The time-varying CIR generated by the simulator is shown in Fig. 7. A group of static multipath components can be observed between the 250th and 500th taps, which represents the acoustic propagation between the source and receiver without the target. A large group of weaker multipath components can be observed with time-varying delays, these are the additional reflections introduced by the moving target. In this simulation scenario, the target crossed the link between the source and the receiver twice. This can be observed from the time-varying

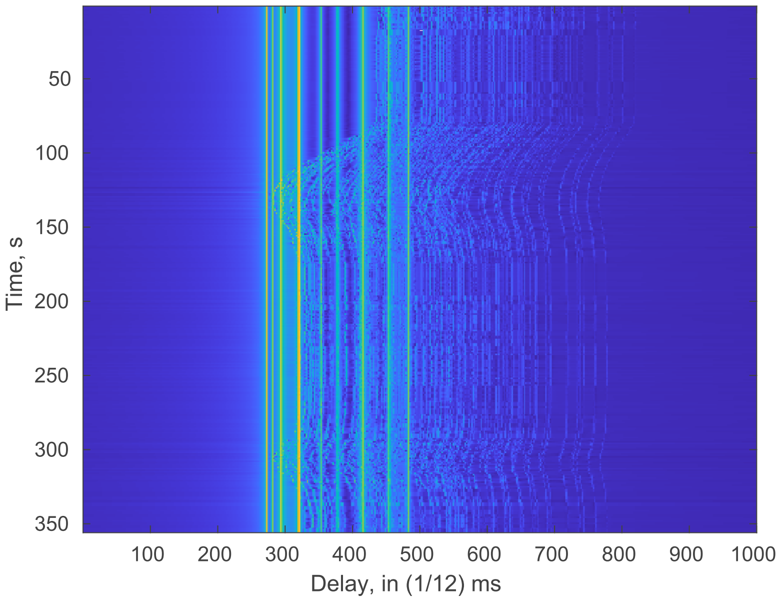

Fig. 7: Time-varying CIR generated by the simulator based on the acoustic field information.

delays of the group of reflections, which reduce when the target is approaching the link and increase as the target moving away from the link.

The time-varying CIR allows us to understand the changes of the CIR structure when a target is crossing the communication link. In practice, channel estimates are obtained by a receiver. A detailed description of the receiver used in this paper can be found in [25]. One of the features of the receiver, useful for the target detection, is the use of turbo iterations for channel estimation and demodulation, resulting in channel estimates obtained using both the pilot and demodulated symbols, thus significantly improving the estimation accuracy compared to the use of the pilot symbols alone. The baseband received signal generated by the simulator is used for channel estimation. The time-varying CIR estimate is shown in Fig. 8. Similar delay variations of the group of reflections is observed when the target is crossing the communication link. This demonstrates that the channel estimator in the receiver is capable of tracking the change of the CIR due to a moving target. In Section VI, this receiver is used for generating the time-varying channel estimate.

The simulator provides a mean to evaluate different algorithms for target detection and has a flexibility of investigating different node configurations within an area of interest. Note that organizing and conducting field experiments with multiple nodes is complicated and expensive; therefore, a simulator for investigation of target detection by a network of nodes is a very

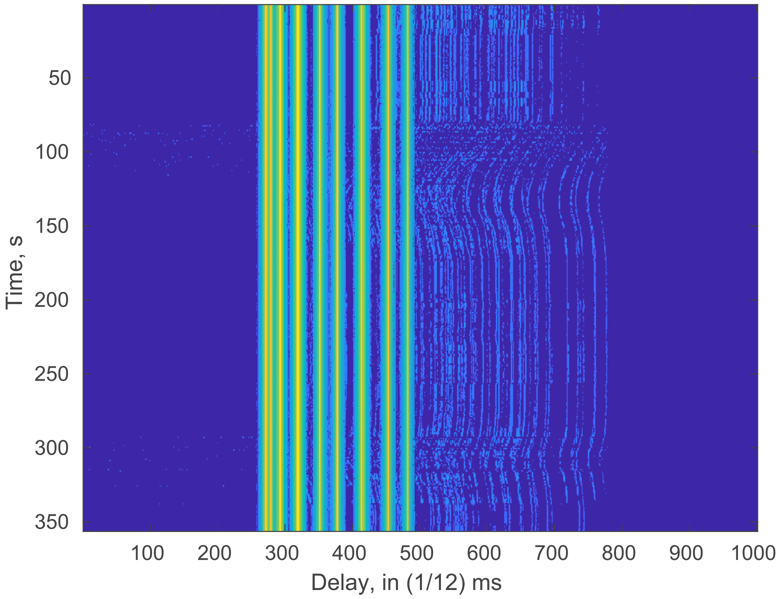

Fig. 8: Time-varying CIR estimate computed using the received signal.

important research tool.

With the two-stage processing, the computational time of simulating the acoustic field for one communication link is significantly reduced. For this simulation, two grid maps are pre-computed. The computation of each grid map takes 25 minutes. For a simulation of 1 s duration, it takes 1.3 minutes to generate the received signal at 12 kHz baseband sampling rate. If the acoustic field is generated directly using BELLHOP3D, it takes about 9 hours to generate 1 s of the received signal with the same sampling rate.

C. *Performance of the proposed detector*

ROC curves are useful for evaluating the performance of a detector. In this section, we show ROC curves of the proposed detector in a number of scenarios.

First, we consider a scenario with a distance between the source and hydrophone about 150 m. The depth of the sea is 12 m. The source position is fixed at 6 m depth. The target is a sphere of 0.2 m radius and it is placed at 8 m depth. Constant sound speed of 1500 m/s is used. In total, we run 10^4 simulation trials. In each trial, the range between the source and the receiver is random and uniformly distributed within [149.9, 150.1] m. The depth of the receiver is random and uniformly distributed within [9.9, 10.1] m. In each trial, a CIR between the source and receiver is generated without the target. Another CIR is generated when the target is fixed in the

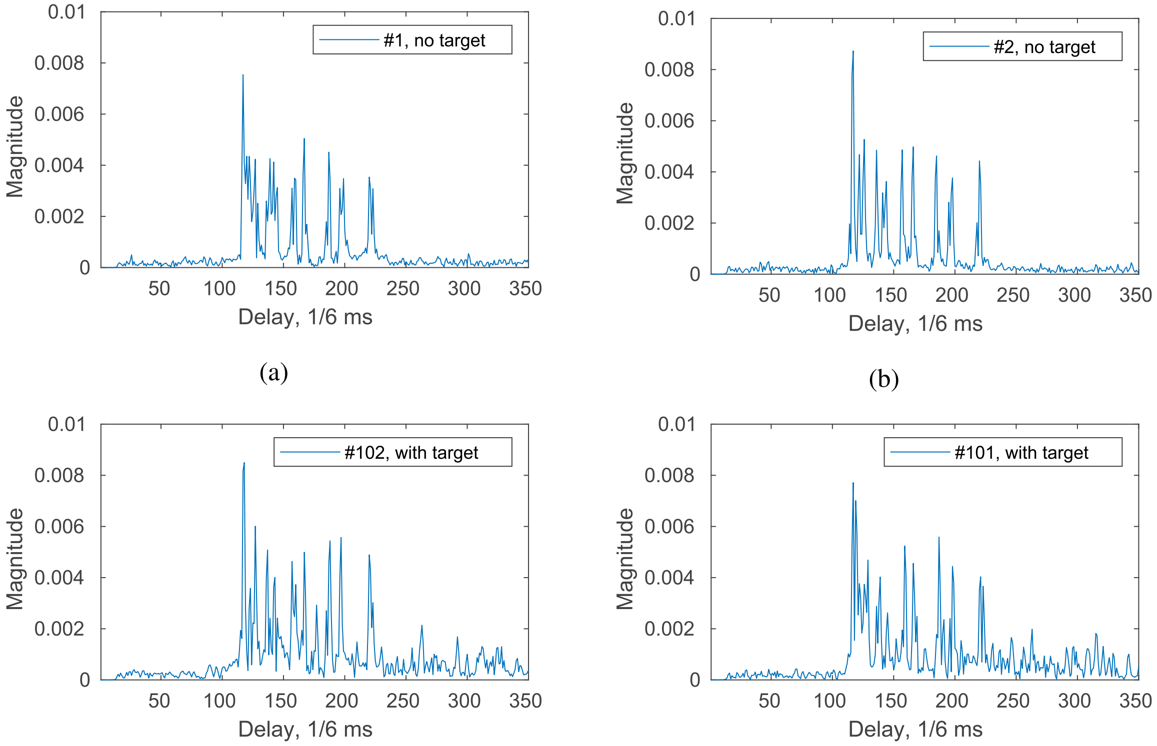

(a) (b) (c) (d)

Fig. 9: Examples of magnitudes of CIR estimates between the source and the receiver. The MSD of the channel estimates is -15 dB. The target is not present in the CIRs shown in (a) and (b). The target is in the middle of the communication link in the CIRs shown in (c) and (d).

middle of the link between the source and a receiver positioned at 150 m range and 10 m depth, whereas the receiver position is random as described above. Thus, we have two datasets of the CIRs, where $\mathcal{D}_0$ contains CIRs without a target and $\mathcal{D}_1$ contains CIRs with a target present. Two example CIRs in $\mathcal{D}_0$ are shown in Fig. 9a and 9b. The multipath structure of these two CIRs are somewhat different due to different receiver positions. The impulse response g in the detection algorithm should deal with the changes in the CIRs due to the receiver motion, otherwise the high normalized MSD between these two CIRs will lead to a false alarm. Two example CIRs in $\mathcal{D}_1$ are shown in Fig. 9c and 9d. A richer multipath structure can be observed compared to the CIRs in $\mathcal{D}_0$.

Independent complex-valued random zero-mean Gaussian numbers of variance σ_n^2 are added to the CIR taps to simulate different levels of the channel estimation accuracy. The channel estimation accuracy is defined in terms of MSD as:

$$\varepsilon = \frac{\sigma_n^2}{\frac{1}{N}\sum_{n=1}^{N} \|\mathbf{h}_n\|_2^2}, \tag{30}$$

where $\mathbf{h}_n$ is the nth CIR in $\mathcal{D}_0$ and $N = 10^4$ is the total number of CIRs. The channel estimation accuracy level ε can be considered as an inverse of a signal-to-noise ratio.

We first investigate the detector performance when the channel estimation accuracy is perfect (ε = $-\infty$ dB). The CIRs from $\mathcal{D}_0$ are used for computing the probability of false alarm against threshold values. For each trial, one CIR is randomly chosen from $\mathcal{D}_0$ as the CIR of interest and $Q = 150$ CIRs are randomly chosen from $\mathcal{D}_0$ as reference CIRs. We consider threshold values Γ between 0 and 1 with a step size of 0.01. The detector outputs are obtained according to (10). The abovementioned process is repeated 2×10^5 times to generate the probability of false alarm against threshold. After that, we compute the probability of detection. For each trial, one CIR is chosen sequentially within $\mathcal{D}_1$ as the CIR of interest, and $Q = 150$ CIRs are randomly chosen within $\mathcal{D}_0$ as reference CIRs. The detector outputs are obtained with the same set of threshold values.

Fig. 10 shows the ROC curves obtained for different length of the filter g, $P = 0, 1$ and 3. When $P = 0$, the filter g is not applied to compensate for the changes caused by environmental factors/node motions in the CIR and the MSD is computed directly using (2). It can be seen that, with $P = 0$, the detector peformance is poor. With $P = 1$, the detector performance is much improved. However, the false alarm rate is still high when the probability of detection is higher than 0.9. With $P = 3$, the detector performance is improved significantly. The probability of detection is higher than 0.9 for a false alarm rate of 10^{-4}. This demonstrates that the filter g can compensate for the channel uncertainty due to the varying receiver positions.

We then investigate the detector performance when using channel estimates of different accuracy. In these simulations, we use $P = 3$. It can be seen from Fig. 11 that the detector performance improves as the MSD level reduces. At a false alarm rate of 10^{-4}, the probability of detection is close to 0.9 when $\varepsilon = -15$ dB, and it is about 0.73 when $\varepsilon = -10$ dB. Note that the channel estimation accuracies we considered here are typical for the channel estimators in communication receivers.

In this work, we consider data packet transmission and the channel between the source and the receiver is measured for every data packet. Here we investigate the influence of the packet transmission rate on target detection in two simulation scenarios at 15 m and 150 m

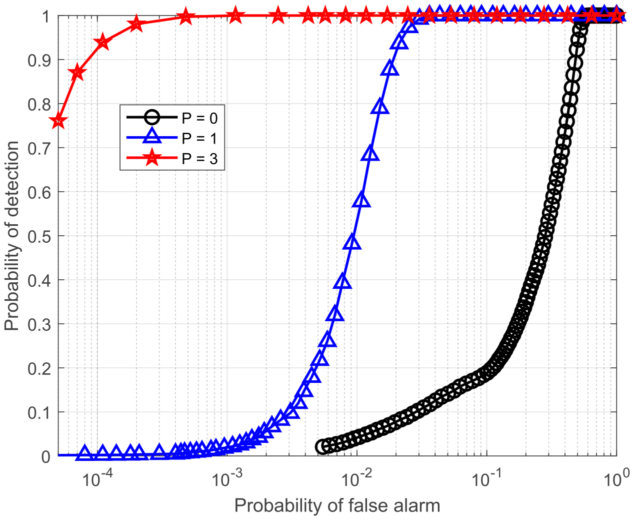

Fig. 10: ROC curves obtained with perfect channel estimates against P.

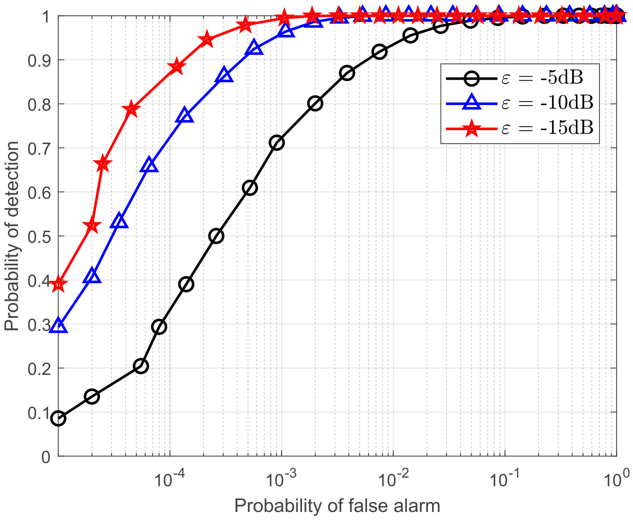

Fig. 11: ROC curves obtained with different channel estimation accuracies; $P = 3$.

communication ranges. In the simulations, the source and the receiver are fixed at 6 m and 10 m depth, respectively. The duration of the transmission is 200 s. The target is moving at 8 m depth with a speed of 1 m/s. The trajectories of the target are shown in Fig. 12. The source (T) is at the same position in both simulations. Hydrophones H1 and H2 are placed at 15 m and 150 m ranges, respectively. The trajectories of the target are shown in black. The starting point of the target is denoted by a green circle and the final position of the target is denoted by a green

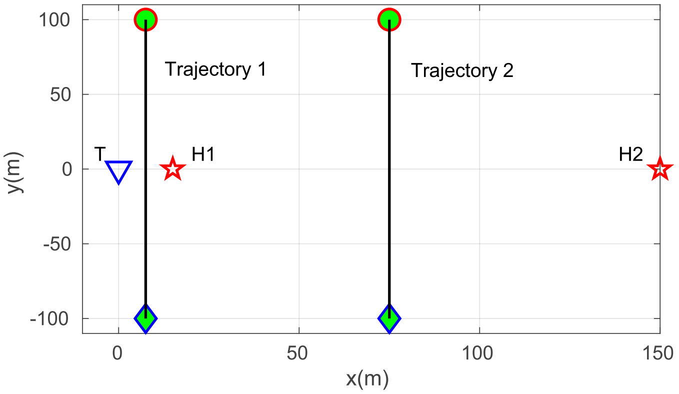

Fig. 12: Configurations of the simulation scenarios at 15 m and 150 m communication ranges. T is the source position; H1 is the hydrophone position in the short-range experiment with the target trajectory 1; H2 is the hydrophone position in the longer-range experiment with the target trajectory 2.

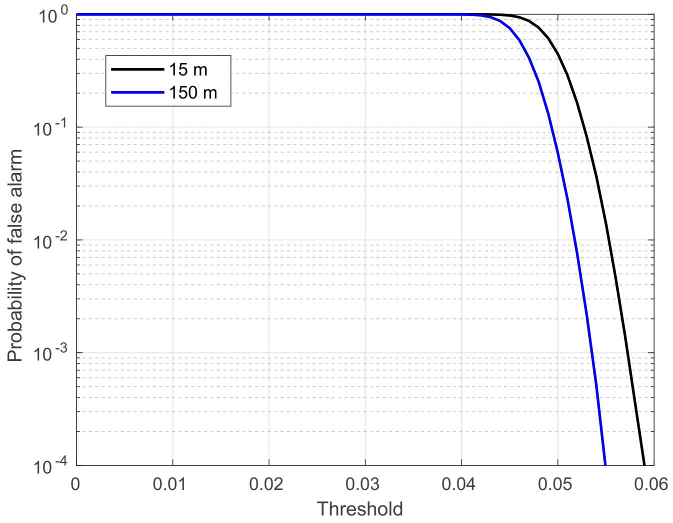

Fig. 13: Probability of false alarm against threshold obtained with $\varepsilon = -15$ dB.

diamond.

During the target motion, the channel between the source and the receiver is measured every 10 ms. In total, 2×10^4 CIRs are generated both with and without the target. The MSD of the channel estimates is -15 dB. $P = 3$ is used in the detection algorithm. Fig. 13 shows the probability of false alarm against threshold. For a false alarm rate of 10^{-4}, the threshold values

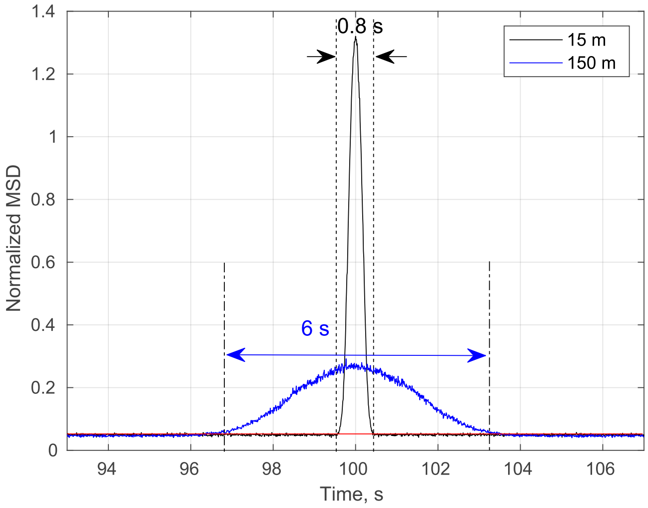

Fig. 14: Normalized MSD obtained in simulations with different ranges of the communication link.

for 15 m and 150 m simulations are 0.055 and 0.059, respectively. The first $Q = 150$ channel estimates when the target is about 100 m away from the communication link are used as the reference CIRs. The normalized MSD (ξ) curves for 15 m and 150 m scenarios are shown in Fig. 14. The red line in Fig. 14 marks the threshold value for the target detection in the 15 m scenario (the higher one). The duration over which the normalized MSD is higher than the threshold is a time window for the target detection. It can be seen that the time window for target detection is 0.8 s for the 15 m range and 6 s for the 150 m range. The length of time window increases as the distance between the source and receiver increases. If we consider a packet transmission rate of one packet per second, we might miss the target for the 15 m range scenario. However, for the 150 m scenario, we have six chances for target detection within the time window.

The time windows for target detection shown in Fig. 14 are obtained when the target is moving at a speed of 1 m/s. If we increase the target speed, the time window for target detection will be reduced. For the simulation scenarios considered here, the data packet transmission rate f_{dp} should satisfy:

$$f_{dp} > 1/\theta, \tag{31}$$

where θ is the duration of the time window. For the 150 m scenario, we have θ = 6 s. Therefore,

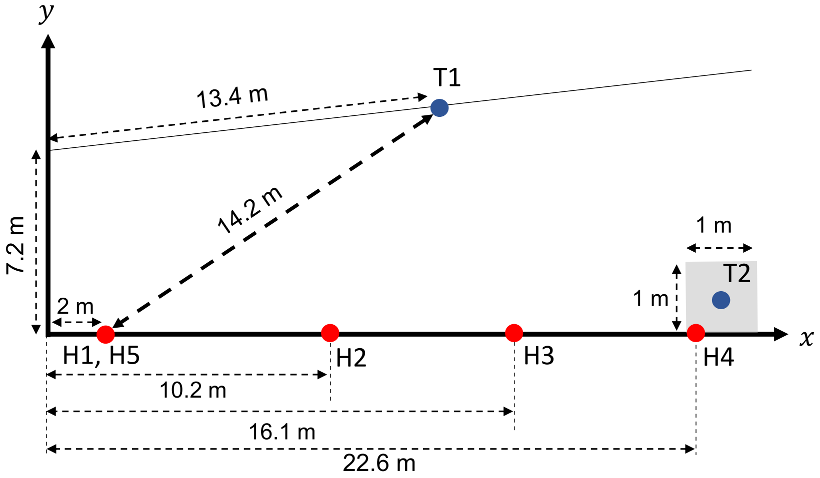

Fig. 15: Configuration of the lake experiment.

the data packet transmission rate f_{dp} should be higher than 0.17 Hz to enable the target to be detected.

VI. LAKE EXPERIMENT

In this section, we describe the lake experiment. Subsection VI-A describes the configuration of the lake experiment. Subsection VI-B introduces the transmitted signal. Subsection VI-C describes the technique used for target trajectory estimation. In subsection VI-D, we demonstrate the target detection capability. Subsection VI-E demonstrates the target detection performance with the simulated data.

A. Experiment setup

The purpose of the lake experiment is to demonstrate the detection of a target crossing a communication link between two nodes. Fig. 15 shows the configuration of the lake experiment. Two projectors (T1 and T2) and five hydrophones (H1 to H5) are deployed. T1 is the source node transmitting data packets of 0.1 s duration and 1 s period at 32 kHz carrier frequency, while T2 is fixed on the target (the yellow buoy in Fig. 16b) transmitting data packets at 24 kHz carrier frequency for the purpose of the acoustic navigation. T1 is fixed at 4.6 m depth. Hydrophones H2 to H5 are fixed at a depth of 1.5 m above the lake bottom. Hydrophone H1 is fixed at a depth of 3 m above the lake bottom. The depth of the lake site varies from 5 m to 8 m depth.

The target is fixed underneath a $1\text{m} \times 1\text{m}$ floating platform shown in Fig. 16a. A weight is attached to the target to ensure it is at approximately 1.5 m depth. During the experiment, a rope

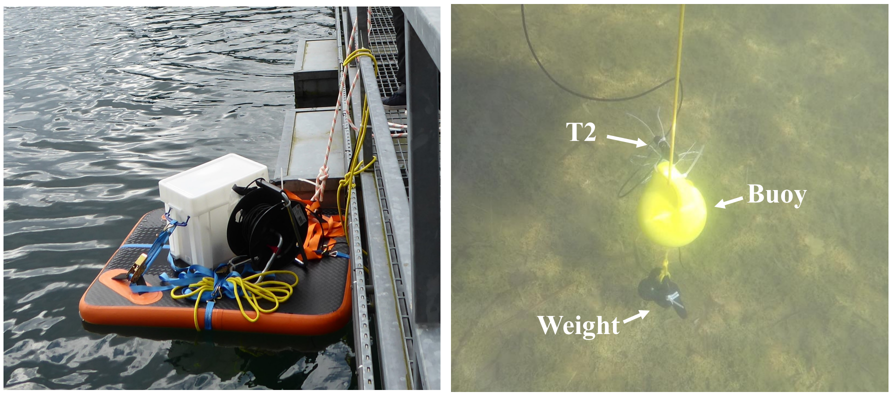

(a) (b)

Fig. 16: Target deployment: (a) floating platform with the acoustic transmitter operating at the carrier frequency 24 kHz for the target navigation; (b) underwater system attached to the floating platform, including the yellow buoy with a weight and projector T2 connected to the transmitter on the top of the floating platform by a cable.

is used to pull the floating platform with the target attached as shown in Fig. 16b diagonally from the point $(22.7, 0)$, near the hydrophone H4, to the point $(1, 7.2)$, or in the opposite direction. The speed of the target movement is about 1 m/s. This target movement was repeated several times during the experiment.

B. Data packet transmission

We consider data packet transmission in the network. A superimposed pilot and data packet structure is used, with pilot symbols $p(i)$ in the real part and data symbols $d(i)$ in the imaginary part [25]. Both the pilot and data are binary phase-shift keying (BPSK) symbols. The data symbols are encoded by a rate 1/3 convolutional code and interleaved. For the transmitted signal, single-carrier modulation is considered. The superimposed pilot and data symbols are pulse-shape filtered and up-sampled by a root raised-cosine (RRC) filter with a roll-off factor of 0.2. After pulse-shaping, the signal is up-converted to the carrier frequency. The data packet duration is 100 ms. In the experiment, the packet transmission rate is one data packet per second.

C. Target trajectory estimation

To evaluate the target detection performance, the ground truth of the target trajectory is required. To accurately estimate the trajectory of the target during the experiment, the projector

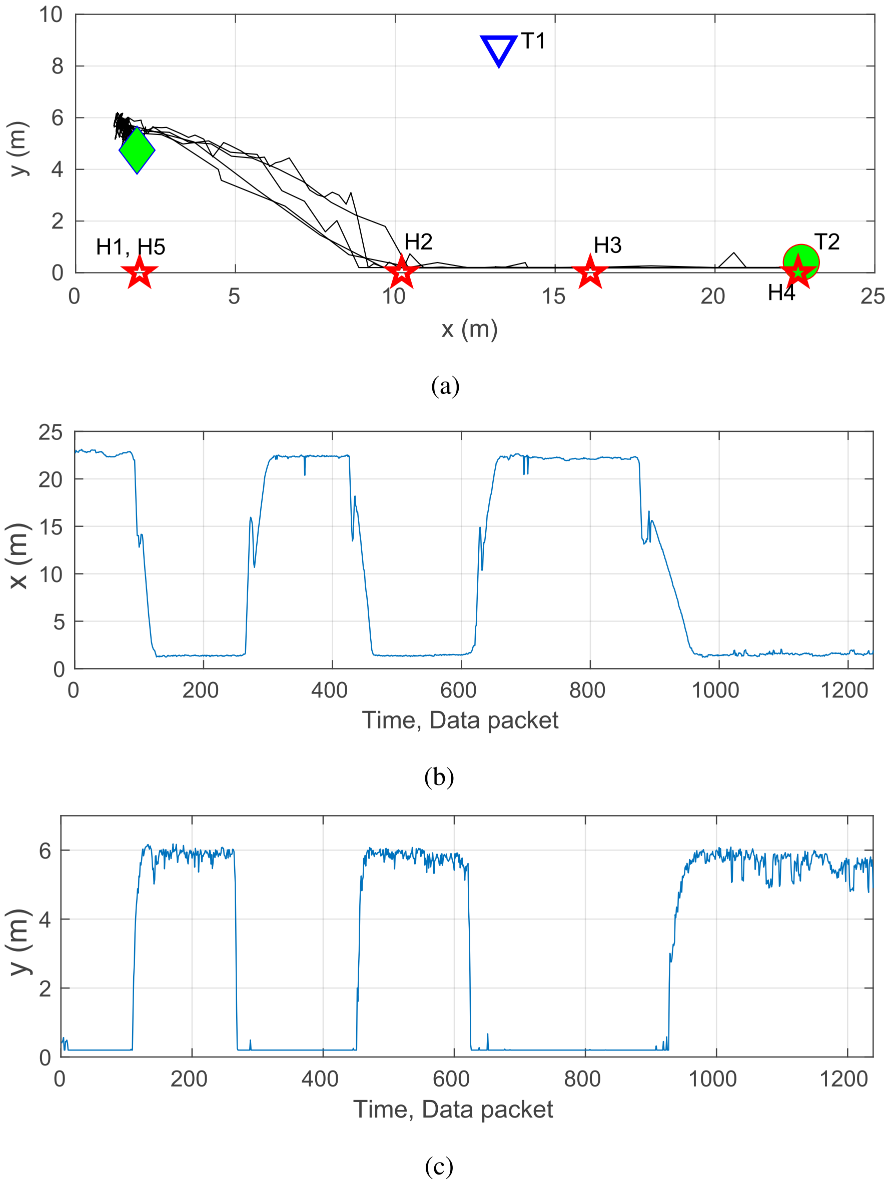

(a)

(b)

(c)

Fig. 17: Coordinate estimates of the target; (a) trajectory of the target during the experiment; (b) x coordinate estimates; (c) y coordinate estimates.

T2 attached to the target transmits the target navigation signal in a frequency band outside of that of the communication signals for the target detection (see Fig. 16b). A simple navigation algorithm is then used based on estimating delays of the first arrivals at the multiple receiving nodes H1 to H5. With the signal bandwidth $F_d = 6$ kHz and oversampling at the receiver to 12 kHz, the delay resolution is 1/12 ms, thus the distance resolution is about 0.1 m, which is good enough for the purpose of the experiment.

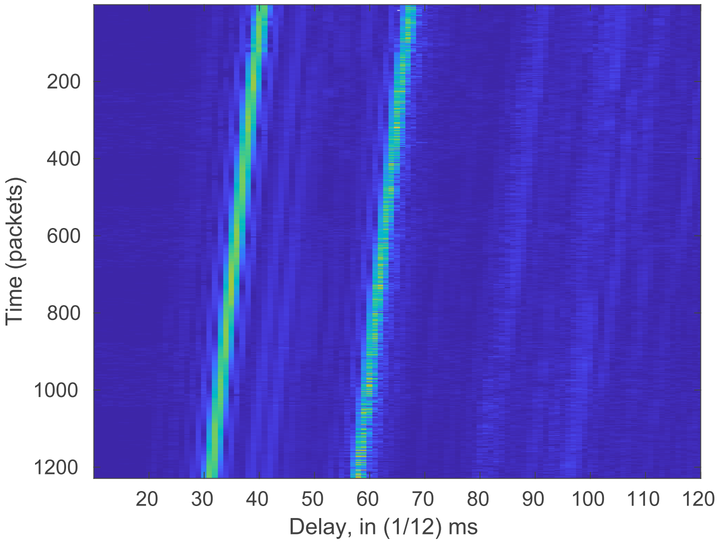

Fig. 18: Channel impulse response between T1 and H5.

Fig. 17a shows the estimated trajectory of the target during the experiment as a black curve. The green circle shows the starting point and the green diamond shows the final position of the target. Fig. 17b and 17c show how the target coordinates x and y, respectively, vary in time. Each slope in Fig. 17b and 17c corresponds to a crossing of the target between the links T1 and H1/H5. The other links are not useful, since the target moves very closely to the other receivers (H2 to H4). Therefore, we use only these two communication links for target detection.

D. *Target detection*

The first step of target detection is to obtain the CIR estimates between T1 and H1 and between T1 and H5, these are available at the receivers. As an example, we show the estimates of the CIR between T1 and H5 in Fig. 18. It can be observed that there is a shift in the delay of the multipath structure over time. This is caused by the unsynchronized clocks on recorders used for data transmission and reception. During the whole transmission interval of about 20 minutes, the delay of the direct path shifted by 0.8 ms. From Fig. 18, it is not possible to visually identify the CIR changes corresponding to the target crossing the communication link.

The normalized MSD during the experiment for all 1200 transmitted data packets according to (9) is plotted in Fig. 19b and 19c for the receivers H1 and H5, respectively. We use the first 50 CIRs and the last 100 CIRs in the experiment, when the target was far from the communication

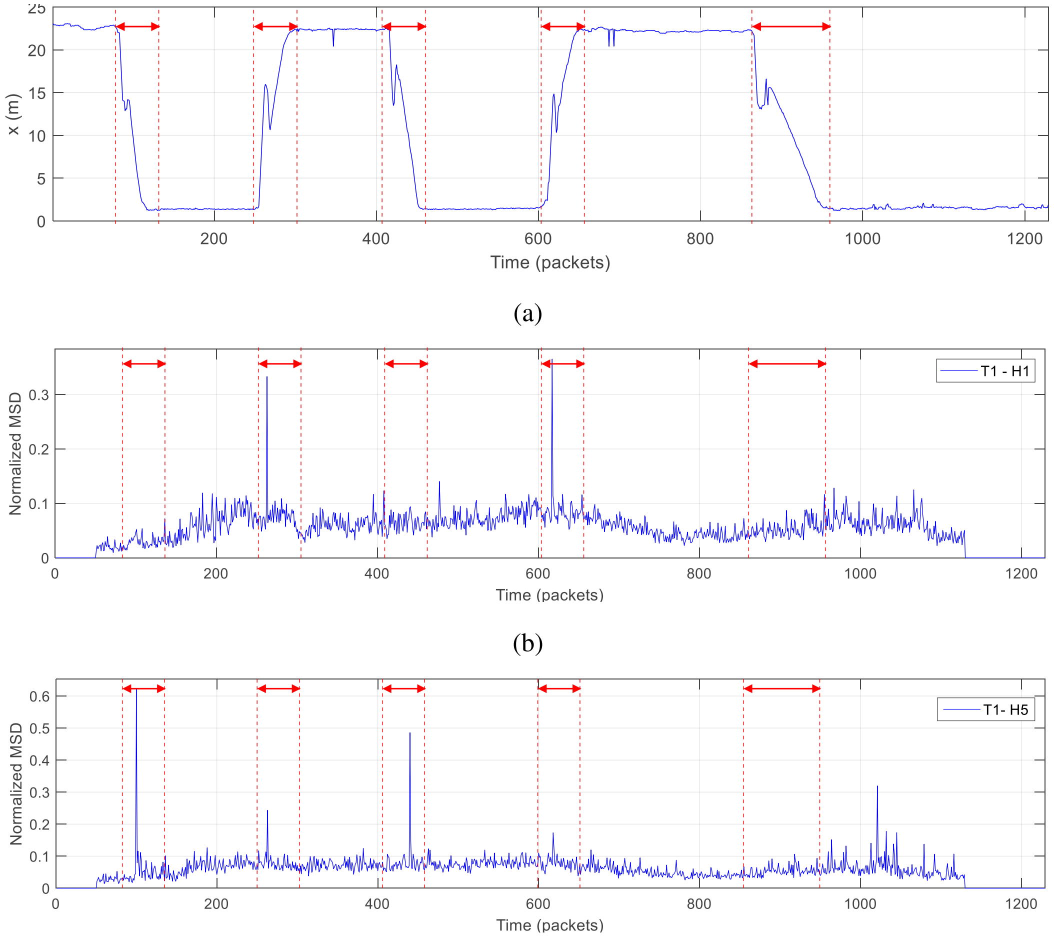

(a)

(b)

(c)

Fig. 19: Normalized MSD in the experiment; (a) x-coordinate estimates; (b) link between T1 and H1; (c) link between T1 and H5.

links of interest, as the reference CIRs. The parameters used in the filter g in (3) are: $P = 10$, $K = 2048$. A large number of taps in the filter g is used to compensate for the delay shift due to the unsynchronized clocks in the recorders and environment variation.

The potential time window of the target crossing is marked with red dotted lines and arrows in Fig. 19. These time windows are chosen based on the changes in the x coordinate estimates. For the channel between T1 and H1, two crossings are detected at the 263th and 617th data packets. For the channel between T1 and H5, two crossings are clearly detected at the 100th and 440th data packets. Two smaller peaks can be observed at the 263th and 618th data packets, which correspond to another two crossings of the target. Due to the one second gap in the data

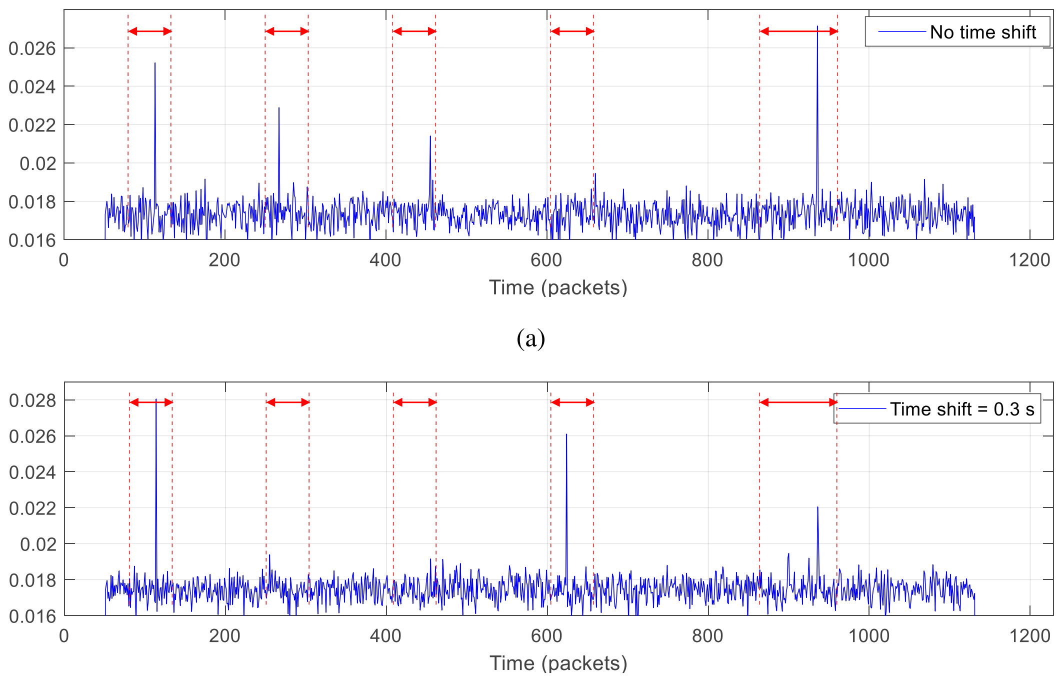

(a)

(b)

Fig. 20: Normalized MSD with the simulated data: (a) Data transmission starts from zero time instant; (b) Data transmission starts from 0.3 s.

packet transmission, it is possible to miss the detection of the target crossing. In this experiment, four out of five target crossings are clearly detected based on the CIRs from H1 and H5. This could be further improved by deploying more hydrophones at different depths and/or reducing the gap between data packet transmissions.

E. Experiment-based simulation

This subsection shows the target detection performance obtained with the simulated data generated based on the setup in lake experiment.

We simulate the channel between T1 and H1. During the experiment, T1 and H1 are located at 4.6 m and 4.4 m depth, respectively. We assume that the target is moving at a depth of 1.5 m at a speed of 1 m/s. The coordinate estimates shown in Fig. 17 are used for interpolating the trajectory of the target during the experiment. The depth of the lake is set to 7 m. Two grid maps are generated at source depths of 1.5 m and 4.6 m. Each grid map covers an area of $35\ \mathrm{m}$

in range and $7\ \mathrm{m}$ in depth. The resolution of the grid map is 1 m in range and 0.5 m in depth. The sound speed in the lake is set based on the temperature of the water (10°) as $c = 1443$ m/s.

The target strength σ_{TS} is computed using (15) with the radius of the target set to 0.1 m. Random Gaussian noise is added to the time-varying CIRs to limit the CIR estimation accuracy at a level of -20 dB in terms of MSD. As there is no issue with the unsynchronized clock in the simulation, we use $P = 1$. We use the first 50 CIRs and the last 100 CIRs in the simulation as the reference CIRs.

Fig. 20 shows the normalized MSD in two experiments. In the first experiment, the data packets are transmitted from zero time instant, while for the second experiment, the transmission starts from 0.3 s. It can be seen that four of five target crossings are detected in the first experiment. In the second experiment three crossings are detected. This is similar to what is observed in the lake experiment. The simulation results demonstrate that the target detection performance is sensitive to the timing of data packet transmissions with respect to the target crossing. This is expected based on the results shown in Fig. 14 for the 15 m range scenario. To increase the possibility of target detection, more frequent data packet transmission or a longer communication range is required.

VII. CONCLUSIONS AND DISCUSSION

In this paper, we have investigated the possibility of target detection by using data transmission between communication nodes in an UWA network. A target detection method has been proposed based on the changes in the time-varying CIRs with respect to reference CIRs obtained without a target. An acoustic simulator has been developed, which is capable of virtual transmission of acoustic signals through a communication link in the presence of a moving target and an approach has been proposed to improve the acoustic field interpolation in the near field. The detector performance has been investigated by simulations in terms of the ROC curves for different channel estimation accurcies. The data packet transmission rate has been analyzed. The detector performance has been further investigated in lake experiments. The proposed detection metric allows clear indication of a moving target crossing a communication link.

The lake experiment considered in this work is of short duration (around twenty minutes). For long term system deployment, the reference CIRs need to be updated frequently based on changes of the acoustic field. The number of reference CIRs used for the detection algorithm also need to be adjusted based on the channel variation uncertainty. A large database of the reference

CIRs when the target is not present are required to compute the false alarm rate against a range of detection thresholds. The threshold used for target detection can be decided based on an acceptable false alarm rate.

Further experiments under different channel conditions are required to understand how to set these parameters in practical scenarios. Sea experiments will be conducted to further validate the detector performance.

REFERENCES

[1] R. Urick, *Principles of Underwater Sound*. Peninsula Publishing, 1983.

[2] Y. Pailhas, Y. Petillot, K. Brown, and B. Mulgrew, “Spatially distributed MIMO sonar systems: principles and capabilities,” *IEEE Journal of Oceanic Engineering*, vol. 42, no. 3, pp. 738–751, 2016.

[3] Y. Pailhas, J. Houssineau, Y. R. Petillot, and D. E. Clark, “Tracking with MIMO sonar systems: applications to harbour surveillance,” *IET Radar, Sonar & Navigation*, vol. 11, no. 4, pp. 629–639, 2017.

[4] V. Zverev, P. Korotin, A. Matveev, V. Mityugov, D. Orlov, B. Salin, and V. Turchin, “Experimental studies of sound diffraction by moving inhomogeneities under shallow-water conditions,” *Acoustical Physics*, vol. 47, pp. 184–193, 2001.

[5] A. Matveev and V. Mityugov, “Determination of the parameters of motion for an underwater object,” *Acoustical Physics*, vol. 48, no. 5, pp. 576–583, 2002.

[6] A. Matveev, D. Orlov, A. Rodionov, B. Salin, and V. Turchin, “Comparative analysis of tomographic methods for the observation of inhomogeneities in a shallow sea,” *Acoustical Physics*, vol. 51, pp. 218–229, 2005.

[7] A. L. Matveev, R. C. Spindel, and D. Rouseff, “Forward scattering observation with partially coherent spatial processing of vertical array signals in shallow water,” *IEEE Journal of Oceanic Engineering*, vol. 32, no. 3, pp. 626–639, 2007.

[8] T. Folegot, G. Martinelli, P. Guerrini, and J. M. Stevenson, “An active acoustic tripwire for simultaneous detection and localization of multiple underwater intruders,” *The Journal of the Acoustical Society of America*, vol. 124, no. 5, pp. 2852–2860, 2008.

[9] B. Lei, Y. Yang, K. Yang, and Y. Ma, “Detection of forward scattering from an intruder in a dynamic littoral environment,” *The Journal of the Acoustical Society of America*, vol. 141, no. 3, pp. 1704–1710, 2017.

[10] N. Morozs, P. D. Mitchell, and Y. Zakharov, “Target detection using underwater acoustic networking,” in *IEEE OCEANS 2023-Limerick*, 2023, pp. 1–5.

[11] N. Morozs, B. Parrein, L. Shen, B. T. Henson, and P. D. Mitchell, “Network protocols for simultaneous underwater acoustic communication and target detection,” in *Proceedings of the Underwater Acoustics Conference and Exhibition (UACE’23), Kalamata, Greece*, 2023.

[12] L. Liao, B. Henson, and Y. Zakharov, “Grid waymark baseband underwater acoustic transmission model,” in *Underwater Acoustics Conference and Exhibition*, 2017, pp. 343–350.

[13] M. Siderius and M. B. Porter, “Modeling broadband ocean acoustic transmissions with time-varying sea surfaces,” *The Journal of the Acoustical Society of America*, vol. 124, no. 1, pp. 137–150, 2008.

[14] A. H. Sayed, *Fundamentals of adaptive filtering*. John Wiley & Sons, 2003.

[15] H. Yu, A. Song, M. Badiey, F. Chen, and F. Ji, “Iterative estimation of doubly selective underwater acoustic channel using basis expansion models,” *Ad Hoc Networks*, vol. 34, pp. 52–61, 2015.

[16] S. Friedberg, A. Insel, and L. Spence, *Linear Algebra*. Pearson Education, 2003.

[17] C. Liu, Y. V. Zakharov, and T. Chen, "Doubly selective underwater acoustic channel model for a moving transmitter/receiver," *IEEE Transactions on Vehicular Technology*, vol. 61, no. 3, pp. 938–950, 2012.

[18] B. Henson, J. Li, Y. V. Zakharov, and C. Liu, "Waymark baseband underwater acoustic propagation model," in *2014 Underwater Communications and Networking (UComms)*. IEEE, 2014, pp. 1–5.

[19] M. B. Porter, "BELLHOP3D User Guide," Heat, Light, and Sound Research, Inc., Tech. Rep., 2016.

[20] R. P. Goddard, "The sonar simulation toolset, release 4.6: Science, mathematics, and algorithms," Washington University Seattle Applied Physics Lab, Tech. Rep., 2008.

[21] "Sonar Acoustics Handbook," Science and Technology Organization Centre for Maritime Research and Experimentation., Tech. Rep., 2016.

[22] K. Li and M. Chitre, "Data-aided underwater acoustic ray propagation modeling," *IEEE Journal of Oceanic Engineering*, vol. 48, no. 4, pp. 1127–1148, 2023.

[23] J. B. Allen and D. A. Berkley, "Image method for efficiently simulating small-room acoustics," *The Journal of the Acoustical Society of America*, vol. 65, no. 4, pp. 943–950, 1979.

[24] N. O. Booth, A. T. Abawi, P. W. Schey, and W. S. Hodgkiss, "Detectability of low-level broad-band signals using adaptive matched-field processing with vertical aperture arrays," *IEEE Journal of Oceanic Engineering*, vol. 25, no. 3, pp. 296–313, 2000.

[25] L. Shen, B. Henson, N. Morozs, Y. Zakharov, and P. D. Mitchell, "Rake receiver with interference cancellation for an underwater acoustic modem," in *Proceedings of the Underwater Acoustics Conference and Exhibition (UACE'23), Kalamata, Greece*, 2023.